PHYSICAL REVIEW B **91**, 214111 (2015)

High-pressure polymorph of $LuFe_2O_4$ with room-temperature antiferromagnetic order

F. Damay,[1,*] M. Poienar,[2] M. Hervieu,[3] A. Guesdon,[3] J. Bourgeois,[1,3] T. Hansen,[4] E. Elkaïm,[5] J. Haines,[2] P. Hermet,[2]
L. Konczewicz,[2] T. Hammouda,[6] J. Rouquette,[2] and C. Martin[3]
[1]*Laboratoire Léon Brillouin, CEA-CNRS UMR 12, 91191 Gif-sur-Yvette Cedex, France*
[2]*Institut Charles Gerhardt, UMR CNRS 5253, Université Montpellier II, Place Eugène Bataillon,*
cc1503, 34095 Montpellier CEDEX 5, France
[3]*Laboratoire CRISMAT, CNRS UMR 6508, 6 boulevard Maréchal Juin, 14050 Caen Cedex, France*
[4]*Institut Laue-Langevin, 6 rue Jules Horowitz, Boîte Postale 156, 38042 Grenoble Cedex 9, France*
[5]*Synchrotron Soleil, L'Orme des Merisiers, Saint-Aubin Boîte Postale 48, 91192 Gif-sur-Yvette Cedex, France*
[6]*Laboratoire Magmas et Volcans, CNRS UMR 6524, 5 rue Kessler, 63038 Clermont-Ferrand Cedex, France*
(Received 15 October 2014; revised manuscript received 10 March 2015; published 23 June 2015)

Branded for its potential electronic ferroelectricity, charge-ordered $LuFe_2O_4$ has a layered Fe triangular framework, whose topology is a source of degeneracy, both at the charge and spin levels. Here we present an in-depth characterization of $LuFe_2O_4$-*hp*, the high-pressure (*hp*) polymorph of $LuFe_2O_4$, using electron, x-ray, and neutron diffraction, combined with transport and magnetization measurements. We show that $LuFe_2O_4$-*hp* is characterized by a *misfit*-related monoclinic structure, accommodating a buckled triangular $[Lu]_\infty$ layer and two shifted adjacent rectangular $[Fe]_\infty$ planes belonging to a distorted rock salt–type layer. The release of the geometric frustration of the Fe magnetic lattice in the *hp* form leads to collinear antiferromagnetic ordering at $T_N = 380\,K$. Possible coexistence of charge and magnetic orders in this material opens research pathways for the design of tunable multifunctional devices using high-pressure techniques.

DOI: 10.1103/PhysRevB.91.214111 PACS number(s): 75.25.Dk, 61.05.cp, 61.50.Ks, 77.80.−e

I. INTRODUCTION

Innovations in high-pressure science have led to the identification of new physical behaviors, such as high-hardness coefficients in B_6O_{1-x} [1], superconductivity in all groups of the periodic table, including rare gases and magnetic metals [2], and optical transparency in light alkali metals such as sodium [3]. In parallel, a new chemistry has flourished, in which high-pressure studies have unveiled previously unknown compounds with unusual atomic coordination and bonding, such as the polymeric forms of N_2 or CO_2 [4,5], or the γ form of the Si_3N_4 spinel, a new wide band-gap semiconductor with rare SiN_6 octahedra [6]. It was recently shown that $LuFe_2O_4$—a potential candidate for ferroelectricity [7,8], mostly known for its complex Fe^{2+}/Fe^{3+} charge ordering (CO) below $T_{CO} = 330\,K$ [9,10],—is transformed under high pressure into a complex orthorhombic phase (denoted hereafter $LuFe_2O_4$-O*hp*), which could be charge ordered at room temperature [11]. The comparison between the properties of polymorphs is often valuable in determining the relevant factors controlling the ground state of a system, in particular when the crystal lattice symmetry implies a high degree of frustration. Our first study of pressure effects on $LuFe_2O_4$ showed that $LuFe_2O_4$-O*hp* is characterized by a large orthorhombic cell [11], resulting from complex twinning mechanisms, and with modulation phenomena, possibly related to charge ordering. In [11], however, the broadening of Bragg peaks owing to the high-pressure experimental conditions prevented any detailed structural information of this form. In this article, detailed synchrotron x-ray, electron, and neutron diffraction studies, combined with density functional theory (DFT) calculations and transport measurements, have been performed on a newly synthesized material, allowing one to revisit the crystal structure of $LuFe_2O_4$-*hp*. In the $LuFe_2O_4$-*hp* phase, although the pseudotriangular lattice of the Lu layer buckles to adapt to the pressure but is preserved, the more deformable Fe bilayer changes to rectangular. $LuFe_2O_4$-*hp* is antiferromagnetic at room temperature, and its magnetic ground state bears close resemblance to that of NaCl-type monoxide FeO [12]. Transport measurements are not conclusive as to whether, and in which temperature range, $LuFe_2O_4$-*hp* could be charge ordered; mixed valence on the rock salt lattice of the Fe bilayer, however, provides ground for further studies on ion transport in this material.

II. EXPERIMENTAL METHODS

$LuFe_2O_4$-*hp* is obtained by irreversible transformation of $LuFe_2O_4$ under high-pressure conditions. Synthesis of $LuFe_2O_4$-*hp* was carried out starting from a $LuFe_2O_4$ powder sample prepared according to the procedure described in [13]. The *in situ* high-pressure synthesis process [14] was followed by neutron diffraction (up to 12 GPa) on the D20 diffractometer (ILL, Grenoble, $\lambda = 1.36$ Å) at ambient temperature (see left panel of Fig. 4). The sample was loaded in a Paris-Edinburgh press, equipped with cubic boron nitride (c-BN) anvils and a Ti-Zr gasket. Pressure was applied using a deuterated 4:1 methanol:ethanol mixture as pressure-transmitting medium.

The $LuFe_2O_4$-*hp* sample recovered from the pressure cell after the pressure release was thereafter used for the synchrotron x-ray and electron diffraction studies, as well as for the neutron diffraction versus temperature study the details of which are given below.

Synchrotron x-ray diffraction was performed on the CRISTAL beamline (Soleil Synchrotron, Saint-Aubin). The powder sample was put in a glass capillary tube of 0.3 mm

---

[*] Corresponding author: francoise.damay@cea.fr

inner diameter, and rotated during the experiment. The data were collected at 300 K, using a wavelength $\lambda = 0.620\,70$ Å.

Electron diffraction (ED) observations were carried out at room temperature, using a JEOL 200 CX microscope, equipped with a tilt-rotation sample holder (±60°). High-resolution electron microscopy was performed with a 2010 FEG microscope. Powder specimens were first crushed in ethanol in an agate mortar; drops of the suspension were subsequently deposited onto a holey carbon grid.

Neutron diffraction experiments versus temperature (in the range 10–730 K) were carried out on the D20 diffractometer with wavelength $\lambda = 2.41$ Å, in a vanadium can. Rietveld refinements of the powder diffraction data were performed with programs of the FULLPROF suite [15].

The $LuFe_2O_4$-*hp* sample used for transport measurements was prepared at Laboratoire Magmas et Volcans: a pressed pellet of $LuFe_2O_4$ was placed in a pressure medium consisting of semisintered Cr-doped MgO, and inserted between eight tungsten carbide anvils with a 1500-ton press. The compression ramp lasted 2 h and the sample was kept at 17 GPa for 2 h. Decompression was achieved in 10 h. Slow decompression is mandatory in order to avoid anvil failure and sample loss. Electrical measurements were performed on a 4 mm × 1.1 mm × 1 mm sample of $LuFe_2O_4$-*hp*. The four electrical contacts located on the boundary of the sample have been made with silver epoxy, and the resistivity value of the sample was measured by a standard dc method in the van der Pauw geometry, taking the average of all current configurations. The current value through the sample has been carefully selected to ensure the ohmicity conditions. The sample holder was placed inside the furnace in a quartz tube, and resistivity measurements were performed under a vacuum of 2.10^{-7} bars. Temperatures of up to 625 K were measured with a platinum Pt resistor and controlled with a precision better than 0.5 K.

Calculations are based on density functional theory and the Perdew, Burke, and Ernzerhof [16] generalized gradient approximation (GGA), as implemented in the VASP code [17,18]. The interactions between ions and electrons were described by the projector augmented-wave method [19]. The plane-wave energy cutoff was 650 eV and the Brillouin zone integration was performed using a 6 × 4 × 2 Monkhorst-Pack mesh [20]. To properly describe the strong electron correlations in iron, the GGA plus on-site repulsion U method (GGA + U), as formulated by Dudarev *et al.* [21], was used with an effective U_{eff} of 4.61 eV. Calculations are spin polarized and performed using a 1 × 2 × 2 supercell to take into account the antiferromagnetic order found experimentally. This supercell is fully relaxed until the maximum residual forces on each atom and pressure are less than 0.003 eV $\mathrm{\AA}^{-1}$ and 0.04 GPa, respectively. Pressure-dependent volume calculated at four pressure values (±0.5 GPa and ±1.0 GPa) were required to derivate the bulk modulus B from the fit of the $B = -V dP/dV$ equation, where V is the cell volume.

III. RESULTS

A. Room-temperature structure of $LuFe_2O_4$-*hp*

The room-temperature (RT) and ambient-pressure $C2/m$ crystal structure of $LuFe_2O_4$ is characterized by a stacking of $[Fe_2O_4]_\infty$ bilayers and CdI_2-type $[LuO_2]_\infty$ layers. The Fe lattice is equivalent to a buckled honeycomb network, also called "W" bilayers [22]. The coordination of Fe inside this bilayer is fivefold (4 + 1) and commonly described as an irregular trigonal bipyramid, with four similar Fe-O distances and a longer one between the Fe planes. It is an example of a lesser common coordination within the vast number of known iron oxides, which tend usually to favor tetrahedral (fourfold) or octahedral (sixfold) environments, like in perovskite- or spinel-related structures. Other examples of fivefold coordination can be found for instance in the $Sr_4Fe_6O_{13-\delta}$ ferrite system [23], in which the Fe cations adopt four different coordination environments, namely, tetragonal pyramid, monocapped tetrahedron, trigonal bipyramid, or octahedron [24].

At ambient temperature and pressure, all the Bragg peaks of the synchrotron x-ray diffraction patterns of $LuFe_2O_4$-*hp* can be indexed using a monoclinic Pm cell, with parameters $a = 5.8045(3)$ Å, $b = 3.2902(2)$ Å, $c = 8.3325(2)$ Å, $\beta = 100.27(6)°$ [Fig. 1(a)]. The reconstruction of the reciprocal space from the electron diffraction (ED) patterns confirms these subcell parameters; the absence of condition of reflection is also consistent with the Pm space group [Fig. 1(b)]. In the [001] ED pattern [Fig. 1(b), middle panel], within

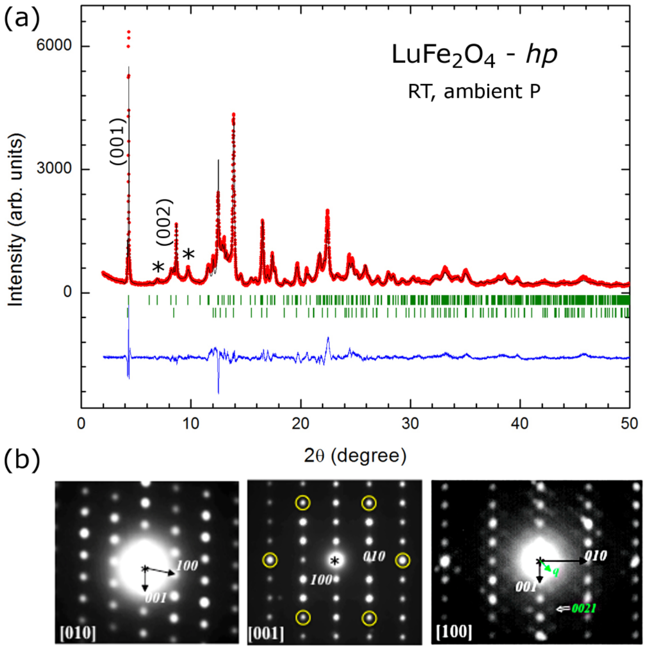

FIG. 1. (Color online) (a) Rietveld refinement profile of the x-ray synchrotron diffraction pattern of the Pm cell of $LuFe_2O_4$-*hp* at 300 K (experimental data: open circles; calculated profile: continuous line; allowed Bragg reflections: vertical marks. The difference between the experimental and calculated profiles is displayed at the bottom of the graph). Stars indicate Bragg intensity resulting from the displacement along c of the Lu positions. The second row of vertical marks corresponds to untransformed $LuFe_2O_4$ [14]. (b) [010], [001], and [100] electron diffraction patterns of $LuFe_2O_4$-*hp*. The circled reflections on the [001] pattern highlight the link with the hexagonal-like $LuFe_2O_4$ phase. The 0021 satellite (using four indices $hklm$ with $m = 1/4b^* + 1/2c^*$) is shown on the [100] pattern.

the rectangular pattern of the Pm reflections, the circled reflections highlight a pseudohexagonal system, reminiscent of the $LuFe_2O_4$ structure. In addition to the intense reflections of the Pm subcell, weak reflections are also observed in the [100] ED pattern [Fig. 1(b), right panel]. They involve a commensurate modulated structure with a propagation vector $1/4b^* + 1/2c^*$, which will be discussed further on.

The high-pressure synthesis process leads to residual structural strains in $LuFe_2O_4$-*hp*, with noticeable anisotropic broadening of the Bragg peaks on the synchrotron x-ray data [Fig. 1(a)]. A search for a structural model was carried out in the Pm cell, focusing first on Lu and Fe atoms, which have the largest x-ray scattering factors. In the Pm cell, there are two Lu sites [1a in $(x\,0\,z)$ and 1b in $(x\,\frac{1}{2}\,z)$] and four Fe sites (two in 1a and two in 1b). Attempts were first based on small shifts (either in-plane or out-of-plane) of the Lu and Fe atoms with respect to their positions in the $LuFe_2O_4$ structure, keeping its overall stacked topology, with slightly distorted or corrugated triangular $[Lu]_\infty$ or $[Fe_2]_\infty$ layers. Not being able to capture the important features of the x-ray pattern, and bearing in mind the recent evidence for the unusual structural flexibility of the iron bilayer with respect to oxygen intercalation [25], a more complicated modeling, involving changes in the topology of the $[Fe]_\infty$ layer, was then attempted. The best refinement is illustrated in Fig. 1(a), with the corresponding cationic framework in Fig. 2(b). The resulting structural model shows that the overall stacking of one $[Lu]_\infty$ and two $[Fe]_\infty$ layers along c is not modified. The Bragg scattering intensity observed for the $(-1\,0\,1)$ and $(-1\,0\,2)$ reflections [stars on Fig. 1(a)] results from the fact that the triangular $[Lu]_\infty$ layer is not planar anymore but strongly corrugated [with Lu atoms in $z = 0$ and $z = 0.138(1)$]. This is further confirmed by high-resolution electron microscopy, as shown by comparing the [010] images of $LuFe_2O_4$ [upper part of Fig. 2(a)] and $LuFe_2O_4$-*hp* [upper part of Fig. 2(b)], images recorded for focus values for which the heavy cations appear as brighter zones. The white dots corresponding to the projection of Lu positions are aligned in Fig. 2(a), but zigzag in Fig. 2(b); in both cases, they perfectly match the calculated positions. Pressure leads therefore to a buckling of the triangular $[Lu]_\infty$ layers, a result that can be understood considering that they are close packed, and therefore quite stable structurally: in PtO_2, the CdI_2-type layers are stable up to 4 GPa at 1500 °C [26]. Similar buckled layers are also found in the metastable form of $LuFeO_3$ [27,28], and in $HgBr_2$ [29].

On the other hand, refinement results of both the x-ray and neutron diffraction data show a major reconstruction of the iron bilayer, involving a change in the topology of the Fe plane from triangular to rectangular [lower parts of Figs. 2(a) and 2(b)]. The Fe-Fe distances extracted from the refinement of the synchrotron x-ray data [Fig. 2(b)] are only qualitative, because of the inherent structural strains and the constraints on oxygen positions. They clearly reflect, nonetheless, the rectangular character of the Fe lattice, with a longer Fe-Fe distance along b, of ∼3.29 Å, and shorter Fe-Fe distances along a, ranging between ∼2.75 and ∼3.05 Å, therefore considerably shorter than the ∼3.44 Å average of the Fe-Fe distances observed in the triangular plane of $LuFe_2O_4$ [Fig. 2(a)] (see also Tables I and II). The stacking of two staggered rectangular Fe planes leads to out-of-plane Fe-Fe distances between ∼3.00 and ∼3.18 Å, for an average of about 3.09 Å, which can be compared with a longer 3.16 Å distance in the original phase (Tables I and II).

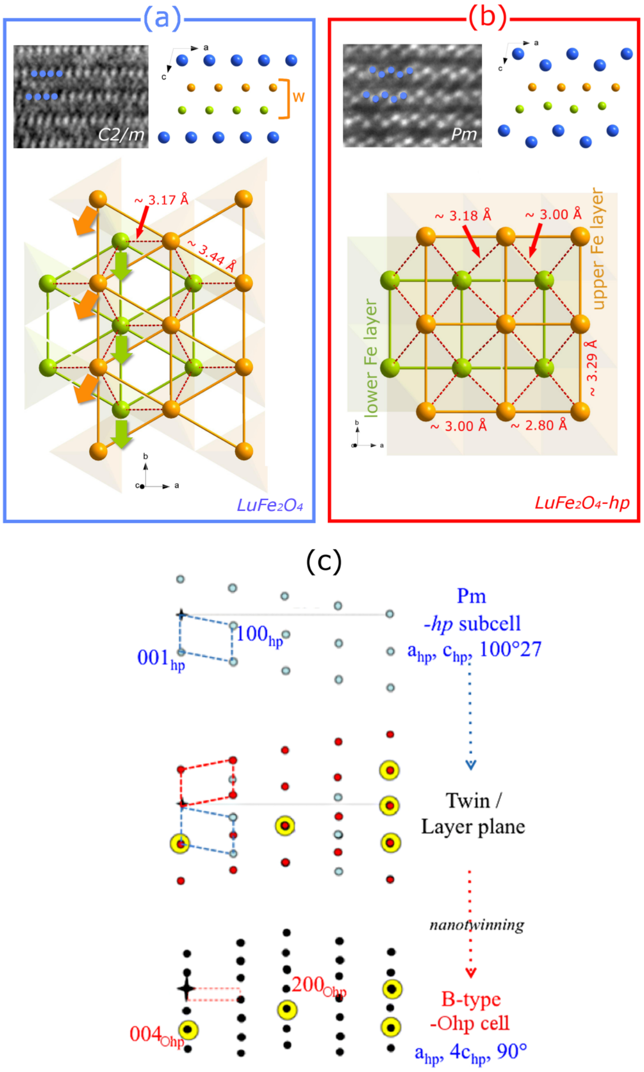

FIG. 2. (Color online) (Top) [010] HREM images; the brighter contrast is associated with the positions of the Lu atoms, zones of higher electron density: the calculated Lu positions in the $C2/m$ [$LuFe_2O_4$, (a)] and Pm [$LuFe_2O_4$-*hp,* (b)] forms are superimposed. In the [010] projections of the crystal structures, Lu atoms are in blue, and Fe atoms in orange and green to differentiate the top and bottom planes of the bilayer. This color code is kept throughout. (Bottom) High-pressure transformation of the initial triangular array of Fe ions (a) to a rectangular one (b), leading to a NaCl-type structure and to an increase (3 → 4) of the in-plane oxygen coordination of Fe. The orange and green arrows schematize the displacements of the iron atoms during the transformation. (c) Structural relationships between the cells of $LuFe_2O_4$-*hp* and $LuFe_2O_4 - Ohp$ [11], following twinning and nanotwining mechanisms (see text), illustrated through the [010] ED patterns. The light blue spots in the upper panel are associated with the reflections of the calculated electron diffraction pattern of the monoclinic Pm cell (blue dashed lines) of $LuFe_2O_4$-*hp*. The system of reflections and the cell resulting from the formation of twins (mirror parallel to the layer plane) and slips are in red (middle panel).

TABLE I. Structural characterization of $LuFe_2O_4$-*hp* at 300 K (from Rietveld refinement of high-resolution synchrotron x-ray powder data). Atoms are on the Wyckoff positions $1a(x,0,z)$ and $1b(x,\frac{1}{2},z)$. The positions of the heavy atomic species Lu and Fe have been determined from synchrotron x-ray data; the positions of oxygen atoms (in italic) have been computed from DFT calculations. Estimated standard deviations were obtained from the Rietveld refinement [15].

Temperature	300 K
Space group	*Pm* (No. 6)
Cell parameters	
a (Å)	5.8045(3)
b (Å)	3.2902(2)
c (Å)	8.3325(2)
β (°)	100.27(6)
Cell volume V(Å^3)	156.59(2)
Lu(1)	(0, 0, 0)
Lu(2)	[0.548(1), 0.5, 0.138(1)]
Fe(1)	[−0.121(4), 0, 0.435(5)]
Fe(2)	[0.353(8), 0, 0.431(4)]
Fe(3)	(0.211(8), 0.5, 0.711(5)]
Fe(4)	[0.687(4), 0.5, 0.685(5)]
O(1)	*(−0.0614, 0, 0.6857)*
O(2)	*(0.4638, 0, 0.6691)*
O(3)	*(0.8189, 0, 0.1940)*
O(4)	*(0.3346, 0, 0.1973)*
O(5)	*(0.6297, 0.5, 0.4387)*
O(6)	*(0.1540, 0.5, 0.4546)*
O(7)	*(0.7618, 0.5, −0.0767)*
O(8)	*(0.2499, 0.5, −0.0652)*
Bragg R factor (%)	8.94
χ^2	5.54

Refining the oxygen positions in $LuFe_2O_4$-*hp* is challenging, considering the eight oxygen sites and the broadening of the Bragg reflections in the diffraction patterns. Simple rectangular oxygen layers seem to be a reasonable hypothesis: the stacking of two shifted $[FeO]_\infty$ planes would form one rock salt–type (RS) layer, leading to an irregular octahedral environment for the Fe atoms and to a sevenfold coordination for Lu akin to the Lu coordination in hexagonal $LuFeO_3$ [27]. Keeping Lu-O and Fe-O distances within the range of those found for hexagonal $LuFeO_3$, this simple structural model gives a good match to the diffraction data. It is also strongly supported by density functional theory calculations. The latter lead to relaxed lattice parameters, $a = 5.935$ Å, $b = 3.250$ Å, $c = 8.519$ Å, and $\beta = 100.53°$, that are 1% − −2% larger than the experimental ones, as usual in GGA. Moreover, the calculated bulk modulus value is 153 GPa, in good agreement with the experimental value $B = 170(6)$ GPa, which was derived from x-ray diffraction experiments under high pressure [14], supporting the validity of the calculated structure. Density functional theory calculations also lead to buckled $[Lu]_\infty$ planes and to an octahedral environment on the four Fe sites (the oxygen positions as determined by DFT are presented in Table I), compressed along the apical bonds and with Fe slightly off-centered (see Table II). It is more realistic, however, to consider that the "true" oxygen network is more complex, with a likely distribution of Fe-O distances on the different Fe sites, a problem that is beyond the power of powder diffraction.

TABLE II. Selected interatomic distances in $LuFe_2O_4$-*hp* at 300 K [from Rietveld refinement of high-resolution synchrotron x-ray powder data and DFT calculations (in italic)]. Estimated standard deviations were obtained from the Rietveld refinement [15].

Distances	(Å)
Lu(1)-Lu(1)/Lu(2)-Lu(2)	3.2902(2)
Lu(1)-Lu(2)	3.464(6)
	3.584(5)
Fe-Fe (in plane)	
Along *a*	2.76(3)
	2.81(3)
	3.01(3)
	3.04(3)
Along *b*	3.2902(2)
Fe-Fe (out-of-plane)	3.02(4)
	3.08(4)
	3.09(4)
	3.18(4)
Fe(1)-O(1)	*2.09*
Fe(1)-O(3)	*1.95*
Fe(1)-O(6) (×2)	*2.20*
Fe(1)-O(5) (×2)	*2.28*

The layered structure of $LuFe_2O_4$-*hp* described here can be compared with the *misfit* crystal structures of cobaltites [30–32], or chalcogenides [33], sometimes synthesized under high pressure [34]. The oxides belonging to this structural family result from the intergrowth of triangular CdI_2- and rectangular RS-type layers (occupied by Co or Cr and alkaline earth, post-transition metals or lanthanides, respectively) and are characterized by strong structural modulations, owing to the discrepancy between the periodicities of the two subsystems. The difference between $LuFe_2O_4$-*hp* and the cobaltites lies in the fact that the transition metal (Fe) is located in the distorted $[FeO]_2$ RS bilayer and the rare earth (Lu) in a buckled CdI_2-like layer. In addition, to accommodate the discrepancy between the two sublattices, the two layers are rotated by about 45° with respect to what is observed in cobaltites. The main originality of $LuFe_2O_4$-*hp* is that, as a result, this adaptability mechanism leads to a *commensurate* match between the Lu triangular and Fe rectangular layers, in contrast with what is generally observed in misfit oxides. Note that the existence, mentioned earlier, of an additional propagation vector $1/4b^* + 1/2c^*$ in $LuFe_2O_4$-*hp*, could originate from charge ordering, as in $LuFe_2O_4$, but could also be linked with a structural modulation originating from the misfitlike character, as such modulations are commonly observed to accommodate two subsystems with different periodicities [33].

B. Relationship with the orthorhombic supercell of $LuFe_2O_4$-O*hp*

In $LuFe_2O_4$-O*hp*, the b_{Ohp}(∼17.5 Å) and c_{Ohp}(∼32.8 Å) cell parameters are multiplied by 5 and 4, respectively, with respect to those of $LuFe_2O_4$-*hp* [11]. The quadrupling of the c_{hp} parameter ($c_{Ohp} \approx 4c_{hp}$) can be explained considering twinning and nanotwinning mechanisms associated with plane slips to release strains. The different steps involved are illustrated in Fig. 2(c). The upper panel of Fig. 2(c) shows part of the [010] ED pattern of the $LuFe_2O_4$-*hp* cell, with $[4\,0\,{-1}]^*$ perpendicular to c^*. In the middle panel is schematized local twinning with regards to this direction in the [010] plane, while the lower panel shows the result of nanotwinning, leading to an angle close to 90° and to a quadrupling of the c parameter, that is, to the B-centered orthorhombiclike cell of $LuFe_2O_4$-O*hp*, with $a_{Ohp} \approx 5.8$ Å $\approx a_{hp}$ and $c_{Ohp} \approx 32$ Å $\approx 4c_{hp}$.

C. Room-temperature magnetic structure of $LuFe_2O_4$-*hp*

Magnetic Bragg peaks are seen in the 300 K neutron diffraction pattern of $LuFe_2O_4$-*hp*, and are characteristic of long-range magnetic ordering [Fig. 3(a)]. These peaks can be indexed with the commensurate propagation vector, $\mathbf{k} = (0\,\frac{1}{2}\,\frac{1}{2})$ [Fig. 3(b)]. From the temperature evolution in the 10–380 K range of the integrated magnetic scattering intensity on the $(0\,0\,0) + \mathbf{k}$ peak, the Néel temperature T_N can be estimated to be around 380 K [Fig. 3(a) and inset]. This value of T_N is confirmed by magnetization measurements (not shown). Symmetry analysis performed on the Pm space group, for the 1a and 1b Fe sites and the $\mathbf{k} = (0\,\frac{1}{2}\,\frac{1}{2})$ propagation vector, shows a constraint on the moment direction, which can be either along b or in the ac plane. Accordingly, the best agreement with the data [Fig. 3(b)] corresponds to Fe moments perpendicular to the ab plane and forming ferromagnetic chains along a, these chains being antiparallel along b [Fig. 3(c), lower part]. At the bilayer level, this magnetic configuration is similar to that of RS-type iron monoxide FeO, whose reported antiferromagnetic spin structure ($T_N \sim 200$ K [12,35]) consists of $(111)_{\text{cubic}}$ planes of ferromagnetic spins [identified by red surfaces on Fig. 3(c)], with an antiferromagnetic coupling between adjacent planes. The bilayers stacking is antiferromagnetic along c [upper part of Fig. 3(c)]. The value of the ordered moment at 310 K is $\sim 4.8(4)\,\mu_B$, which would agree with a 1:1 ratio of Fe^{2+} and Fe^{3+} species in their high-spin (HS) states. This result

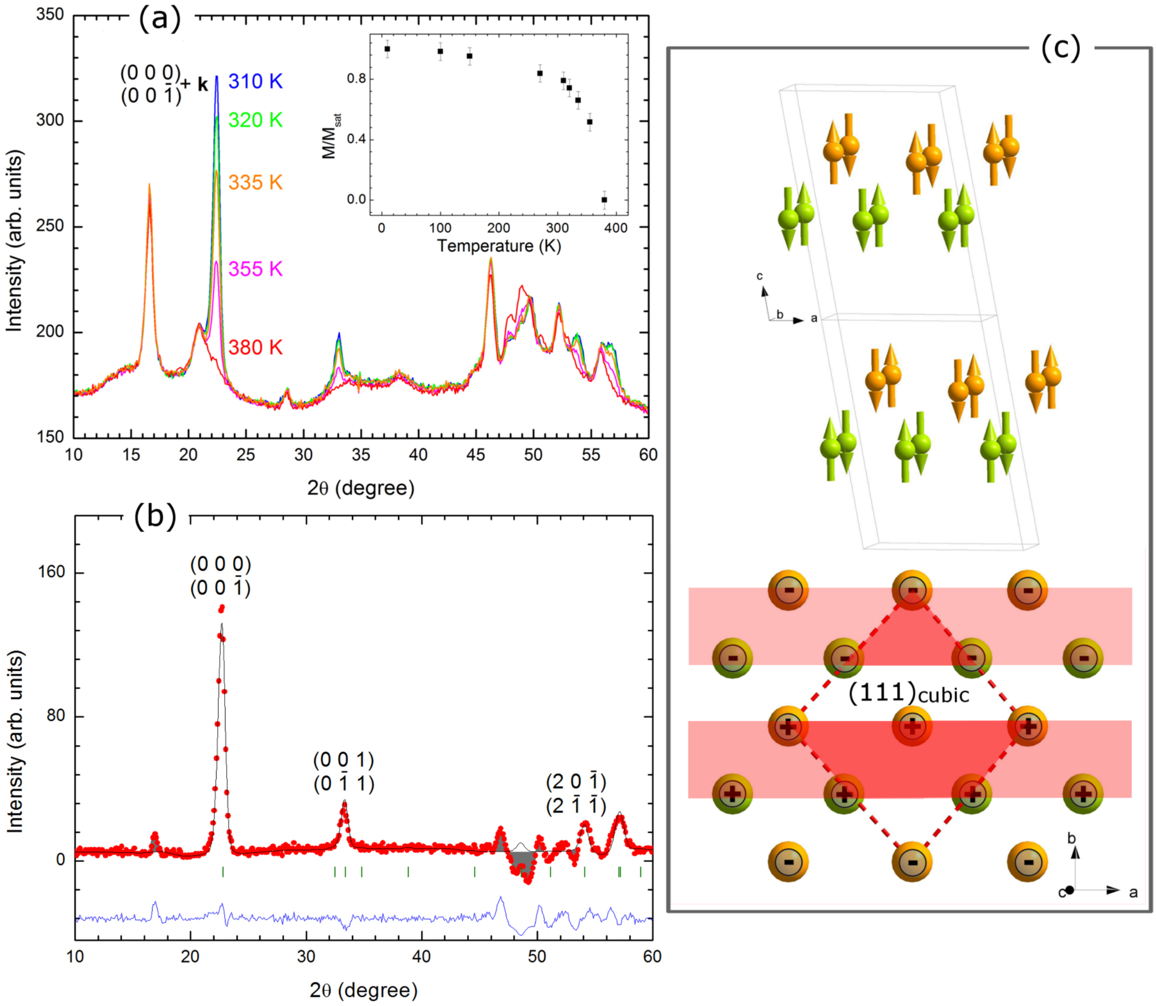

FIG. 3. (Color online) (a) Neutron diffraction patterns of $LuFe_2O_4$-*hp* in the 310–380 K range. Inset: evolution of the normalized magnetic moment (with respect to the 10 K value) with temperature. (b) Observed (red circles), calculated (solid line), and difference (bottom line) magnetic intensity profile of $LuFe_2O_4$-*hp* (gray areas correspond to artifacts at crystal Bragg peaks positions). (c) Perspective view of the $LuFe_2O_4$-*hp* antiferromagnetic structure and projection of a single RS layer in the ab plane, showing the comparison with the FeO magnetic order (red dotted line), corresponding to ferromagnetic $(111)_{\text{cubic}}$ planes (outlined in red) coupled antiferromagnetically.

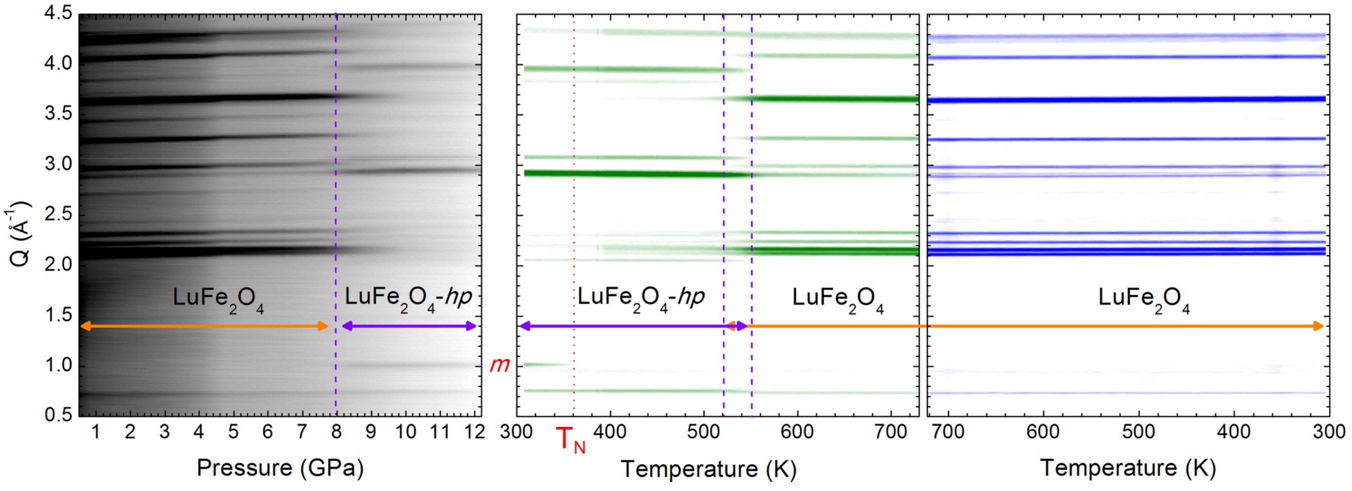

FIG. 4. (Color online) (From left to right) Evolution with pressure (at RT), increasing temperature (from RT to 730 K, in vacuum), and decreasing temperature (from 730 K back to RT, in vacuum) of the neutron diffraction patterns, showing the structural phase transition $LuFe_2O_4$ → $LuFe_2O_4$-*hp* around 8 GPa, and its reversibility ($LuFe_2O_4$-*hp* → $LuFe_2O_4$, starting around 520 K in vacuum). Arrows in orange (purple) indicate the pressure or temperature range in which $LuFe_2O_4$($LuFe_2O_4$-*hp*) is identified on the diffraction patterns. The dotted red line marks the antiferromagnetic transition temperature of $LuFe_2O_4$-*hp*, and the red letter m the position in Q of the corresponding main antiferromagnetic Bragg peak.

would agree with the fact that HS to low-spin (LS) transitions are generally observed at much higher pressures [36,37], but Mössbauer experiments would be needed at this point to further investigate the Fe atoms' local environments and spin state.

D. Reversibility of the $LuFe_2O_4$-*hp* → $LuFe_2O_4$ transition at high temperature

The pressure-induced structural transition, around 8 GPa, from as-synthesized $LuFe_2O_4$ to $LuFe_2O_4$-*hp*, followed by neutron diffraction at 300 K, is illustrated in the left panel of Fig. 4. The middle panel of Fig. 4 shows the evolution with increasing temperature of the $LuFe_2O_4$-*hp* phase between 300 and 730 K. $LuFe_2O_4$-*hp* is stable up to ~400 K, the temperature at which weak intensities corresponding to the $LuFe_2O_4$ phase are observed in the neutron diffraction patterns. The $LuFe_2O_4$-*hp* → $LuFe_2O_4$ transformation accelerates between 520 and 550 K, and from 550 up to 730 K, only single-phase $LuFe_2O_4$ is observed in the neutron diffractograms. In the right panel of Fig. 4, which shows the evolution of diffractograms with decreasing temperature from 730 to 300 K, no additional structural changes are observed down to RT. This confirms that $LuFe_2O_4$-*hp* is a metastable structural form at ambient pressure, which transforms back to $LuFe_2O_4$ after mild temperature treatment above 400 K.

E. Transport properties of $LuFe_2O_4$-*hp* versus temperature

Transport $\rho(T)$ measurements were performed to get further insight on a possible CO state in the $LuFe_2O_4$-*hp* phase (Fig. 5). In $LuFe_2O_4$, $T_{CO} \sim 330\,K$ can be easily identified on the $\rho(T^{-1})$ curve, as it is accompanied by a change in the conductivity regime (gray dots in Fig. 5). For $LuFe_2O_4$-*hp* (purple dots), whose resistivity at 300 K is an order of magnitude larger than as-synthesized $LuFe_2O_4$, a steady decrease of resistivity is observed as temperature increases (purple arrow 1), with a 20% drop around 410 K, possibly linked with the antiferromagnetic ordering transition. There is no noticeable change in the conduction regime at T_N or above and the activation energy estimated from a simple Arrhenius law leads to 430 meV in both the paramagnetic and antiferromagnetic states. The resistivity jump around 530 K (dotted red arrow) corresponds to the phase transition back to the $LuFe_2O_4$-type structure, as supported by the neutron diffraction data (Fig. 4, middle panel).

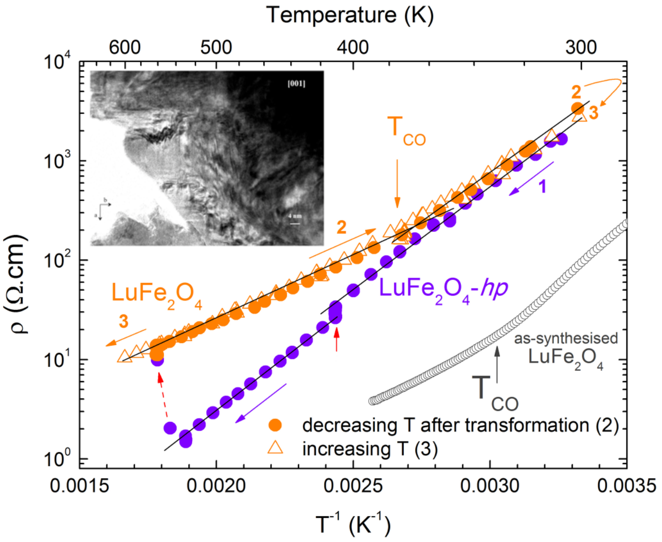

FIG. 5. (Color online) Temperature evolution of the resistivity ρ of the $LuFe_2O_4$-*hp* sample heated in vacuum ($P = 2.10^{-7}$ bars) up to 565 K (1, full purple circles), then cooled down to RT after transformation into $LuFe_2O_4$ (2, full orange circles), and heated up again to demonstrate reproducibility (3, hollow orange triangles). $\rho(T)$ of the as-synthesized $LuFe_2O_4$ is also shown (hollow gray circles) for comparison purposes. Inset: [001] bright-field image of $LuFe_2O_4$-*hp*.

After the structural transition (orange curves) to $LuFe_2O_4$, the $\rho(T^{-1})$ evolution bears close resemblance to that of as-synthesized $LuFe_2O_4$. The two activation energy regimes that can be identified, as in as-synthesized $LuFe_2O_4$, are therefore likely related to the occurrence of charge ordering. The transport properties are reproducible in this temperature range, as can be seen from the comparison between the data measured with increasing (orange arrow labeled 2 and corresponding orange dots) or decreasing (orange arrow labeled 3 and corresponding orange hollow triangles) temperature. Interestingly, the charge-ordering temperature is higher in the $LuFe_2O_4$ compound resulting from the transformation of the $-hp$ phase, around $T_{CO} \sim 380$ K, than in as-synthesized $LuFe_2O_4$ ($T_{CO} \sim 330$ K). In contrast, the activation energies in the two conductivity regimes, either above or below T_{CO}, are close in both samples (whether as-synthesized or resulting from the transformation of the $-hp$ phase). The difference by an order of magnitude of the resistivity at 300 K between the two $LuFe_2O_4$ samples of Fig. 5 is likely related with the degraded microstructural state of the $LuFe_2O_4$-*hp*, which is retained after transformation into $LuFe_2O_4$ despite the temperature treatment. This is illustrated by the uneven contrast observed in the bright-field images of the crystallites viewed along [001] in the inset of Fig. 5.

IV. DISCUSSION

Under specific conditions, such as thin-film deposition on chosen substrates [38] or high pressure [39], polymorphic mechanisms have been observed in hexagonal manganites $RMnO_3$, which are characterized by a single layer of MnO_5 trigonal bipyramids. In $LuMnO_3$, for instance, the hexagonal to orthorhombic phase transformation involves a significant motion of the O atoms within the *ab* plane. Hexagonal ferrites can be stabilized on specific substrates also [40], but examples illustrating the effect of pressure on the coordination of FeO_5 bipyramids are rarely found in the literature. Although not an oxide, $ZnIn_2S_4$ [41] is worth mentioning, as it has the same structure as $LuFe_2O_4$. Its high-pressure form is a cubic spinel, in which there is an increase of the coordination of In atoms, from 5 in the W layer, to 6 in the octahedral sites of the spinel. On the other hand, the coordination of the Zn atoms changes from 5 in the W layer to 4 in the spinel (tetrahedral sites).

Structurally, the effects induced by pressure on the $LuFe_2O_4$ framework are rather unique, as they combine two different responses to an external stress : the original CdI_2 layer is preserved, albeit buckled, whereas the W bilayer undergoes a profound restructuration to form a rectangular bilayer. The decrease of the cell parameters of $LuFe_2O_4$-*hp* with respect to $LuFe_2O_4$ is particularly pronounced along *b*, which is shortened by more than 4%. The variation of the cell volume is of about −9%, in agreement with the values reported for other examples of high-pressure structural transformations [42,43]. The coexistence of both polymorphs during the high-pressure synthesis process, the discontinuity of the cell parameters and volumes, and metastability are all indicative of a first-order transition. The breakage of primary interatomic bonds and changes in atomic coordinations further indicates a transition of the reconstructive type, following Buerger's classification of structural phase transitions [44]. It results in an original phase, belonging to the misfitlike structures, built from rotated rectangular RS and triangular CdI_2-like layers. A thorough understanding of the actual reconstructive transformation pathways [45,46] is beyond the scope of this article.

Unlike $LuFe_2O_4$ [47], there is no obvious sign of two-dimensional magnetism in $LuFe_2O_4$-*hp*. In fact, in view of the complexity of the magnetic ground state reported for $LuFe_2O_4$ [48,49], the magnetic properties of $LuFe_2O_4$-*hp* are arresting. There is no particular broadening of the magnetic peaks, as would be expected in case of short-range correlations, nor an increasing broadening of the peaks with the scattering angle, as can be seen in $LuFe_2O_4$ itself [48], and which is attributed to magnetic stacking disorder along *c*. Moreover, the increase of T_N in the $-hp$ phase ($T_N = 250$ K in $LuFe_2O_4$) also underlines an increase of the magnetic exchange constants, possibly linked with the loss of the two-dimensional magnetic character of $LuFe_2O_4$ in the *hp* phase, and/or with larger exchange constants within the bilayers, through an increase of the Fe d_{x2-y2} and O *p* orbitals' hybridization in the high-pressure form. The fact that the iron spin keeps an axial anisotropy perpendicular to the basal plane despite the change in its environment is an interesting characteristic of the phase, with potential consequences on its magnetostriction properties.

$LuFe_2O_4$ is presently at the center of a controversy concerning its ferroelectric properties [50] and the alleged role of charge ordering, and the question arises as to whether $LuFe_2O_4$-*hp* can exhibit either. In $LuFe_2O_4$, the most conclusive evidences of CO were a change of slope in the $\rho(T)$ curve and superstructures reflections below T_{CO} on ED patterns. It is difficult to ascertain the existence of CO based on the resistivity measurements of $LuFe_2O_4$-*hp* performed in this work, but electron diffraction on the other hand clearly shows complex structural modulations in the *hp* phase, with a propagation vector $1/4b^* + 1/2c^*$ reminiscent of the extra reflections associated with CO in $LuFe_2O_4$ (involving modulation vectors within the *bc* plane of the monoclinic structure [13]). Moreover, DFT calculations actually yield a magnetic structure similar to the one determined experimentally, with an additional modulation of the ordered moment amplitude, depending on the Fe valence (this modulation does not improve the refinement of the neutron diffraction data significantly and was therefore not implemented in the latter): The CO derived from these calculations would correspond to alternating stripes of Fe^{3+} and Fe^{2+} parallel to *b*. The presence of four different Fe sites in the *Pm* cell of $LuFe_2O_4$-*hp* can actually accommodate this type of CO without any additional superstructure, and the link between the modulation vector determined by electron diffraction and a CO state remains therefore uncertain. Demonstrating the existence of CO in $LuFe_2O_4$-*hp* will therefore require further studies, with the motivating possibility of a new misfit structure with room-temperature coexistence of charge and antiferromagnetic orders. In addition, alongside the recent observation of remarkable oxygen intercalation properties in $LuFe_2O_4$ [25], the existence in $LuFe_2O_4$-*hp* of mixed-valence $[FeO]_2^{RS}$ layers, similar to those found in ion conductor $Sr_4Fe_6O_{13-\delta}$ [23], extends the potential of this compound towards mixed ion conductivity or oxygen permeability applications.

V. CONCLUSION

A crystal structure is proposed for the high-pressure polymorph of $LuFe_2O_4$, based on extensive synchrotron x-ray, neutron, and electron diffraction experiments. $LuFe_2O_4$-*hp* exhibits a monoclinic crystal structure, with a stacking of buckled triangular $[Lu]_\infty$ and rectangular $[Fe]_\infty$ layers, akin to *misfit* structures. Antiferromagnetic ordering, characterized by ferromagnetic chains coupled antiferromagnetically, occurs below 380 K. Unlike $LuFe_2O_4$, no conclusive sign of charge ordering can be inferred from the transport properties versus temperature, although DFT calculations indicate that a CO phase could be stable. $LuFe_2O_4$-*hp* is metastable at ambient pressure and reverts to $LuFe_2O_4$ around 530 K.

ACKNOWLEDGMENTS

The authors acknowledge G. Hearne (University of Johannesburg) and A. Maignan (CRISMAT) for discussions. The multianvil apparatus of Laboratoire Magmas et Volcans is financially supported by the Centre National de la Recherche Scientifique (Instrument National de l'INSU). Financial support for this work was partially provided by the French Agence Nationale de la Recherche, Grants No. ANR-08-BLAN-0005-01 and No. JC08-331297.

---

[1] H. Hubert, B. Devouard, L. A. J. Garvie, M. O'Keeffe, P. R. Buseck, W. T. Petuskey, and P. F. McMillan, Nature **391**, 376 (1998).

[2] P. F. McMillan, Nat. Mater. **1**, 19 (2002).

[3] Y. Ma, M. Eremets, A. R. Oganov, Y. Xie, I. Trojan, S. Medvedev, A. O. Lyakhov, M. Valle, and V. Prakapenka, Nature **458**, 182 (2009).

[4] E. Gregoryanz, A. F. Goncharov, R. J. Hemley, and H. K. Mao, Phys. Rev. B **64**, 052103 (2001).

[5] V. Iota, C. S. Yoo, and H. Cynn, Science **283**, 1510 (1999).

[6] A. Zerr, G. Miehe, G. Serghiou, M. Schwarz, E. Kroke, R. Riedel, H. Fuess, P. Kroll, and R. Boehler, Nature **400**, 340 (1999).

[7] N. Ikeda, H. Ohsumi, K. Ohwada, K. Ishii, T. Inami, K. Kakurai, Y. Murakami, K. Yoshii, S. Mori, Y. Horibe, and H. Kito, Nature **436**, 1136 (2005).

[8] S. W. Cheong and M. Mostovoy, Nat. Mater. **6**, 13 (2007).

[9] Y. Yamada, K. Kitsuda, S. Nohdo, and N. Ikeda, Phys. Rev. B **62**, 12167 (2000).

[10] Y. Zhang, H. X. Yang, C. Ma, H. F. Tian, and J. Q. Li, Phys. Rev. Lett. **98**, 247602 (2007).

[11] J. Rouquette, J. Haines, A. Al-Zein, P. Papet, F. Damay, J. Bourgeois, T. Hammouda, F. Dore, A. Maignan, M. Hervieu, and C. Martin, Phys. Rev. Lett. **105**, 237203 (2010).

[12] W. L. Roth, Phys. Rev. **110**, 1333 (1958).

[13] J. Bourgeois, M. Hervieu, M. Poienar, A. M. Abakumov, E. Elkaim, M. T. Sougrati, F. Porcher, F. Damay, J. Rouquette, G. Van Tendeloo, A. Maignan, J. Haines, and C. Martin, Phys. Rev. B **85**, 064102 (2012).

[14] M. Poienar (unpublished).

[15] J. Rodriguez-Carvajal, Phys. B **192**, 55 (1993).

[16] J. P. Perdew, K. Burke, and M. Ernzerhof, Phys. Rev. Lett. **77**, 3865 (1996).

[17] G. Kresse and J. Furthmuller, Comput. Mater. Sci. **6**, 15 (1996).

[18] G. Kresse and J. Hafner, Phys. Rev. B **47**, 558 (1993).

[19] G. Kresse and D. Joubert, Phys. Rev. B **59**, 1758 (1999).

[20] H. J. Monkhorst and J. D. Pack, Phys. Rev. B **13**, 5188 (1976).

[21] S. L. Dudarev, G. A. Botton, S. Y. Savrasov, C. J. Humphreys, and A. P. Sutton, Phys. Rev. B **57**, 1505 (1998).

[22] N. Kimizuka, E. Takayama-Muromachi, and K. Siratori, in *Handbook on the Physics and Chemistry of Rare Earths*, Vol. 13, edited by K. A. Gschneider, Jr. and L. Eyring (Elsevier Science B.V., Amsterdam, 1990), Chap. 90, p. 283.

[23] A. Yoshiasa, K. Ueno, F. Kanamaru, and H. Horiuchi, Mater. Res. Bull. **21**, 175 (1986).

[24] O. Perez, B. Mellenne, R. Retoux, B. Raveau, and M. Hervieu, Solid State Sci. **8**, 431 (2006).

[25] M. Hervieu, A. Guesdon, J. Bourgeois, E. Elkaim, M. Poienar, F. Damay, J. Rouquette, A. Maignan, and C. Martin, Nat. Mater. **13**, 74 (2014).

[26] K.-J. Range, F. Rau, U. Klement, and A. Heyns, Mater. Res. Bull. **22**, 1541 (1987).

[27] E. Magome, C. Moriyoshi, Y. Kuroiwa, A. Masuno, and H. Inoue, Jpn. J. Appl. Phys. **49**, 09ME06 (2010).

[28] W. Wang, J. Zhao, W. Wang, Z. Gai, N. Balke, M. Chi, H. N. Lee, W. Tian, L. Zhu, X. Cheng, D. J. Keavney, J. Yi, T. Z. Ward, P. C. Snijders, H. M. Christen, W. Wu, J. Shen, and X. Xu, Phys. Rev. Lett. **110**, 237601 (2013).

[29] M. Hostettler, D. Schwarzenbach, J. Helbing, V. Dmitriev, and H. P. Weber, Solid State Commun. **129**, 359 (2004).

[30] P. Boullay, B. Domenges, M. Hervieu, D. Groult, and B. Raveau, Chem. Mater. **8**, 1482 (1996).

[31] T. Nagai, K. Sakai, M. Karppinen, T. Asaka, K. Kimoto, A. Yamazaki, H. Yamauchi, and Y. Matsui, J. Solid State Chem. **179**, 1898 (2006).

[32] M. Shizuya, M. Isobe, Y. Baba, T. Nagai, M. Osada, K. Kosuda, S. Takenouchi, Y. Matsui, and E. Takayama-Muromachi, J. Solid State Chem. **180**, 249 (2007).

[33] G. A. Wiegers, Prog. Solid State Chem. **24**, 1 (1996).

[34] E. Castillo-Martinez, A. Schoenleber, S. van Smaalen, A. M. Arevalo-Lopez, and M. A. Alario-Franco, J. Solid State Chem. **181**, 1840 (2008).

[35] C. G. Shull, W. A. Strauser, and E. O. Wollan, Phys. Rev. **83**, 333 (1951).

[36] M. Merlini, M. Hanfland, M. Gemmi, S. Huotari, L. Simonelli, and P. Strobel, Am. Mineral. **95**, 200 (2010).

[37] R. E. Cohen, I. I. Mazin, and D. G. Isaak, Science **275**, 654 (1997).

[38] P. A. Salvador, T. D. Doan, B. Mercey, and B. Raveau, Chem. Mater. **10**, 2592 (1998).

[39] P. Gao, Z. Chen, T. A. Tyson, T. Wu, K. H. Ahn, Z. Liu, R. Tappero, S. B. Kim, and S.-W. Cheong, Phys. Rev. B **83**, 224113 (2011).

[40] A. A. Bossak, I. E. Graboy, O. Y. Gorbenko, A. R. Kaul, M. S. Kartavtseva, V. L. Svetchnikov, and H. W. Zandbergen, Chem. Mater. **16**, 1751 (2004).

[41] N. Berand and K. J. Range, J. Alloys Compd. **241**, 29 (1996).
[42] R. D. Shannon and C. T. Prewitt, Mater. Res. Bull. **4**, 57 (1969).
[43] G. Demazeau, Z. Naturforsch., B: J. Chem. Sci. **61**, 799 (2006).
[44] J. Buerger, *Phase Transformation in Solids* (Wiley, New York, 1951).
[45] H. T. Stokes, D. M. Hatch, J. J. Dong, and J. P. Lewis, Phys. Rev. B **69**, 174111 (2004).
[46] C. Capillas, J. M. Perez-Mato, and M. I. Aroyo, J. Phys.: Condens. Matter **19**, 275203 (2007).
[47] J. Iida, Y. Nakagawa, S. Funahashi, S. Takekawa, and N. Kimizuka, J. Phys. Coll. **49**, C8-1497 (1988).
[48] J. Bourgeois, G. André, S. Petit, J. Robert, M. Poienar, J. Rouquette, E. Elkaim, M. Hervieu, A. Maignan, C. Martin, and F. Damay, Phys. Rev. B **86**, 024413 (2012).
[49] J. de Groot, K. Marty, M. D. Lumsden, A. D. Christianson, S. E. Nagler, S. Adiga, W. J. H. Borghols, K. Schmalzl, Z. Yamani, S. R. Bland, R. de Souza, U. Staub, W. Schweika, Y. Su, and M. Angst, Phys. Rev. Lett. **108**, 037206 (2012).
[50] J. de Groot, T. Mueller, R. A. Rosenberg, D. J. Keavney, Z. Islam, J. W. Kim, and M. Angst, Phys. Rev. Lett. **108**, 187601 (2012).